Materials Characterization 168 (2020) 110524

Contents lists available at ScienceDirect

Materials Characterization

journal homepage: www.elsevier.com/locate/matchar

Friction stir welding of 2060–T8 Al—Li alloy. Part I: Microstructure evolution mechanism and mechanical properties

Y. Tao, Z. Zhang*, B.H. Yu, P. Xue, D.R. Ni, B.L. Xiao, Z.Y. Ma*

Institute of Metal Research, Chinese Academy of Sciences, Shenyang 110016, China

ARTICLE INFO

Keywords:
Friction stir welding
Aluminum–Lithium alloys
Precipitates
Hardness
Strength
Fracture

ABSTRACT

2 mm thick rolled 2060–T8 Al—Li alloy plates were subjected to friction stir welding (FSW) under rotation rates of 400–1200 rpm and welding speeds of 50–200 mm/min. In the nugget zone (NZ), FSW resulted in the dissolution of the precipitates and the formation of δ′ (Al_3Zr) precipitates, as well as the formation of Guinier–Preston (GP) and Guinier–Preston–Bagaryatsky (GPB) zones except for at 400 rpm–200 mm/min. In the heat affected zone (HAZ), FSW led to the dissolution and coarsening of T_1 (Al_2CuLi) and S′ (Al_2CuMg), and the subsequent formation of new θ′ (Al_2Cu) and σ ($Al_5Cu_6Mg_2$) precipitates. The lowest hardness zones (LHZs) of the FSW joints were located at either the NZ or the HAZ under varied welding parameters. Different from the FSW joints of conventional precipitation–hardened aluminum alloys, the ultimate tensile strength of FSW 2060–T8 joints increased as the rotation rate increased from 400 to 800 rpm, but was unchanged with further increasing the rotation rate from 800 to 1200 rpm under a constant welding speed of 200 mm/min. On the other hand, the joint strength increased as the welding speed increased from 50 to 200 mm/min under a constant rotation rate of 1200 rpm. While the FSW joints fractured at the LHZs under 400 rpm–200 mm/min and 1200 rpm–50 mm/min, abnormal fracture at the thermo–mechanically affected zone (TMAZ) was observed under 800 rpm–200 mm/min and 1200 rpm–200 mm/min.

1. Introduction

Due to the outstanding combination of properties, such as high specific strength, specific stiffness, as well as excellent fatigue resistance and fracture toughness, the third generation of aluminum–lithium (Al—Li) alloys have been developed recently, targeting for applications in aerospace industry for the sake of weight saving [1,2]. However, Li element evaporation, gas cavities and solidification cracks are unavoidable in the fusion welds of Al—Li alloys due to melting and re-solidification under high heat input, degrading the mechanical properties of the fusion welds [3].

Friction stir welding (FSW), characterized by the plastic flow without melting of base material (BM), is a new alternative welding technology for the difficult–to–weld materials [4–7]. Owing to absence of melting and solidification processes and low heat input during FSW, the problems resulting from the fusion welding process could be avoided in the FSW joints. Thus, FSW is considered to be a feasible welding technology for the Al—Li alloys.

Under the stirring action of the rotating tool during the FSW process, the material undergoes the varied degrees of heat input and plastic deformation on the transverse section from the weld center to both the retreating side (RS) and the advancing side (AS), producing three distinct regions: nugget zone (NZ), thermo–mechanically affected zone (TMAZ) and heat affected zone (HAZ) [8]. Generally, for conventional precipitation–hardened (2xxx, 6xxx, and 7xxx) aluminum alloys, FSW resulted in the dissolution and coarsening of precipitates in the HAZ, which is the lowest hardness zone (LHZ) and plays a crucial role in determining the mechanical properties and fracture behavior of the FSW joints [9,10].

In recent years, the third generation of the Al—Li alloys has been subjected to extensive FSW investigations, parts of which are summarized in Table 1 [11–19]. Compared to the FSW joints of conventional 2xxx, 6xxx, and 7xxx aluminum alloys, the FSW Al—Li alloy joints exhibited unique characteristics in the microstructure evolution, mechanical properties and fracture behavior.

Firstly, the microstructure evolutions of the FSW Al—Li alloy joints were complicated and systematic investigations are lacking. Investigations of FSW joints of 2098–T8 [1], 2195–T8 [11,12], 2198–T8 [13,14], 2199–T8 [15] and 2050–T8 [16] indicated that most of the precipitates dissolved in the NZ and TMAZ while the dissolution and coarsening of precipitates occurred in the HAZ. For the FSW 2060–T8 joints, Mao et al. [17], Yan et al. [18], Liu et al. [19] and Cai

* Corresponding authors.
E-mail addresses: zhangzhen@imr.ac.cn (Z. Zhang), zyma@imr.ac.cn (Z.Y. Ma).

https://doi.org/10.1016/j.matchar.2020.110524
Received 23 March 2020; Received in revised form 8 June 2020; Accepted 11 July 2020
Available online 16 July 2020

Table 1
Existent precipitates in various zones of FSW Al—Li joints.

Alloy	Rotation rate (rpm)	Welding speed (mm/min)	Precipitates				Location of LHZ	Fracture location	Ref.
			BM	NZ	TMAZ	HAZ			
2198–T8	800, 1600	200	T1, θ′, δ′	δ′	–	–	HAZ	NZ	[23]
2195–T8	2200, 2400	75, 150	T1, θ′, S′, δ′	δ′	–	T1, δ′	HAZ	NZ	[12]
2060–T8	750–1500	95–150	–	T1 + S′ or δ′ + β′	–	–	HAZ	NZ or HAZ	[17]
2060–T8	400–1300	100	T1, θ′, S′, δ′, β′	T or δ′ + β′	–	–	HAZ	NZ	[18]
2060–T8	600–1000	300	T1, θ′, S′, δ′, β′	T1 or δ′ + β′	–	–	HAZ	NZ	[19]
2060–T8	2400	100	T1, θ′, S′	Cu–Mg clusters	σ	–	HAZ	NZ/TMAZ	[20]

Table 2
Welding parameters of FSW 2060–T8 joints.

Sample	Rotation rate (R), rpm	Welding speed (V), mm/min	Designation
1	400	200	400–200
2	800	200	800–200
3	1200	200	1200–200
4	1200	50	1200–50

et al. [20] found that the precipitates of the NZ might be T ($Al_{20}Cu_2Mn_3$), T_1 (Al_2CuLi), T_1 + S′ (Al_2CuMg) or δ′ (Al_3Li) + β′ (Al_3Zr) under the varied welding parameters. Cai et al.'s study [20] indicated that T_1, θ′ (Al_2Cu) and S′ precipitates were completely dissolved and cubic shaped σ ($Al_5Cu_6Mg_2$) precipitates appeared in the TMAZ of FSW 2060–T8 joints at 2400 rpm–100 mm/min. Nevertheless, the effect of welding parameters on the precipitate evolution of the TMAZ and HAZ of FSW 2060 Al–T8 joints was lack of investigations.

Secondly, the joint strength variation with the welding parameters for the Al—Li alloys is different from that for conventional 2xxx, 6xxx, and 7xxx aluminum alloys, where the joint strength increased with increasing the welding speed and was not affected by the rotation rate [21,22]. Tao et al. [23] reported that the ultimate tensile strength (UTS) of the FSW 2198–T8 joints decreased with increasing the rotation rate. Mao et al. [17], Yan et al. [18] and Liu et al. [19] found that the UTS of the FSW 2060–T8 joints first increased and then decreased with increasing the rotation rate or welding speed. However, the relationship between welding parameters and UTS of FSW Al—Li alloy joints were lack of detailed mechanism explanation.

Thirdly, the FSW Al—Li alloy joints exhibited abnormal fracture behavior at non–LHZ region, whereas for conventional 2xxx, 6xxx, and 7xxx aluminum alloys, the FSW joint failure usually occurred at the LHZ. The failures at the LHZ and non–LHZ region were designated as normal and abnormal fractures, respectively. For example, for FSW 2195–T8 joints [12] and FSW 2198–T8 joints [23], although the LHZs were located at the HAZ, failure abnormally occurred in the NZ, which is reported to result from the low Taylor factor and lithium segregation at grain boundaries in the NZ by Tao et al. [23]. Similarly, FSW 2060–T8 joints frequently exhibited abnormal fracture locations at the NZ or the NZ/TMAZ interface instead of the LHZs (HAZ) [1,17–19], however the reason for abnormal tensile fracture behavior of FSW 2060–T8 joints has not been reported.

The above studies indicated that FSW 2060–T8 joints exhibited the different characteristics in the mechanical properties and fracture behavior under the varied welding parameters. It should be noted that thinning of the as–FSW joints is unavoidable in order to ensure the joint quality. Thus, when using as–FSW 2060–T8 joints to test, the intrinsic mechanical properties and fracture behavior could not be revealed because of the varied cross–sectional area at various locations of the joints as shown in previous studies [1,12,16–21]. Therefore, a systematical study aimed at elucidating the intrinsic relationship of precipitate evolution, mechanical properties, abnormal fracture behavior and welding parameters for FSW 2060–T8 joints is indispensable.

In this investigation, 2060–T8 alloy was friction stir welded under rotation rates of 400–1200 rpm and welding speeds of 50–200 mm/min and subjected to detailed microstructural analyses and mechanical property evaluation. The objective of the present work is to (a) understand the microstructural evolution behavior of 2060–T8 alloy during FSW and its effect on the intrinsic mechanical properties of the FSW joints under a wide range of welding parameters and (b) elucidate the intrinsic tensile fracture behavior of FSW 2060–T8 joint. (a) is reported in this article, while (b) will be described in a companion article.

2. Experimental procedure

2 mm thick rolled 2060–T8 Al—Li alloy sheets with a composition of Al–0.70Li–3.76Cu–0.72Mg–0.33Ag–0.30Mn–0.35Zn–0.12Zr (wt%) were used in this study. The sheets, with a length of 400 mm and a width of 100 mm, were cleared by abrasive papers on the top surfaces and butt surfaces, and then were butt welded along the rolling direction using a FSW machine under rotation rates of 400–1200 rpm and welding speeds of 50–200 mm/min, which are shown in detail in Table 2. A tool with a concave shoulder 12 mm in diameter and a threaded cone–shaped pin 4 mm in root diameter and 1.85 mm in length was used. The FSW samples were designated in brief forms. For example, sample 1200–200 denotes the sample welded at a rotational rate of 1200 rpm and a welding speed of 200 mm/min.

Before welding, the zero point of the welding tool along the thickness direction was set accurately. Based on FSW experience, the plunge depths were set as 0.15 mm for all the FSW samples. In order to keep the plunge depth constant, the welding tool reached the setting plunge depth and then rotated for 5 s before traveling along the welding direction. Moreover, the plunge depth remained unchanged for all FSW processes in this work. All the FSW samples were naturally aged at room temperature for more than 2 months before precipitate characterization and hardness tests.

Vickers hardness measurement was conducted on the cross section perpendicular to the welding direction using an automatic testing machine (LECO, LM–247AT, LECO Corporation, St. Joseph, MI, USA) under a load of 500 g for 10 s. The hardness profiles of the joints were obtained along the mid–thickness of the cross section at an interval of 1 mm.

All the joints were cross sectioned perpendicular to the welding direction using an electrical discharge machine (DK7732, Kedi CNC Machine Tool Co., Ltd., Taizhou, China). Metallographic observation was carried out by optical microscopy (OM, Axiovert 200 MAT, Carl Zeiss. Inc., Oberkochen, Germany). The specimens for OM were ground and polished and then etched using Keller's reagent (190 ml water, 2 ml hydrofluoric acid, 3 ml hydrochloric acid and 5 ml nitric acid).

The microstructures of FSW joints were characterized using transmission electron microscopy (TEM TECNAI20, FEI Company, Hillsboro, Oregon, USA). Thin foils for TEM observation were cut from corresponding locations in the weld using an electrical–discharge machine, and were then prepared by jet electro polishing using a solution of 75 pct methanol and 25 pct nitric at 248 K (−25 °C) and 10 V. Precipitate distributions were characterized by the combination of selected area diffraction (SAD) patterns, bright field imaging and dark field imaging

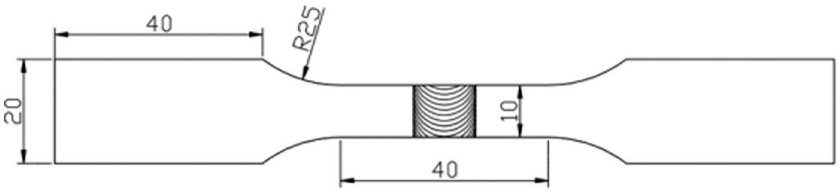

Fig. 1. Configuration and size of tensile specimen.

techniques of TEM.

The FSW samples for tensile tests were cross sectioned perpendicular to the welding direction using an electrical discharge machine. In order to obtain the intrinsic mechanical properties and fracture behavior of the joints, the joint surfaces for the tensile specimens were planed with abrasive papers to insure the equal cross–sectional area at various locations of the joints. The configuration and size of the transverse tensile specimens are shown in Fig. 1. Room–temperature tensile tests were carried out using the Zwick–Roell testing machine at a strain rate of 1.0×10^{-3} s^{-1} and the tensile properties of each joint reported were the averages of three test results.

3. Results

3.1. OM microstructure characteristics

Fig. 2 shows the cross–sectional macrostructure of the FSW 2060–T8 joint. No welding defect was detected for all the FSW 2060–T8 joints under investigated FSW parameters. Three zones; i.e., NZ, TMAZ, and HAZ, were discernible. The TMAZ could be divided into two sub–zones (marked by arrows in Fig. 2) according to the grain characteristics, i.e., upper TMAZ and lower TMAZ, which were mainly influenced by the shoulder and stirring pin during FSW, respectively.

Fig. 3 shows the OM micrographs of the BM, HAZ, upper TMAZ and lower TMAZ of sample 1200–200. It can be seen that the elongated grains of the BM resulting from the rolling process were 100–200 μm long and approximately 10–50 μm wide (Fig. 3a). In the HAZ, the slightly coarsened grains were observed (Fig. 3b). Compared with those in the BM, the grains were longer and thinner at the upper TMAZ but were shorter and coarser at the lower TMAZ (Fig. 3c and d).

Fig. 4 shows the OM micrographs of the NZ of the FSW 2060–T8 joints. It can be seen that the grain size of the NZs for samples 400–200, 800–200, 1200–200 and 1200–50 were 1.8, 3.5, 5.0 and 7.5 μm (Fig. 4a–d), respectively. This indicated the occurrence of dynamic recrystallization in the NZs under the severe plastic deformation and thermal exposure. Increasing the rotation rate from 400 to 1200 rpm under a constant welding speed of 200 mm/min or decreasing the welding speed from 200 to 50 mm/min under a constant rotation rate of 1200 rpm led to increase of grain size in the NZ of the FSW 2060–T8 joints.

3.2. Microhardness

Fig. 5 shows the microhardness profiles of FSW 2060–T8 joints under different welding parameters. Generally, the hardness of the FSW joints was much lower than that of the BM. The effect of the rotation rate on the hardness profiles of the FSW joints under a constant welding speed of 200 mm/min is shown in Fig. 5a. For sample 400–200, although the hardness distribution in the NZ is relatively uniform, an indistinctive LHZ was observed in the NZ, the hardness of which was only slightly lower than that of the TMAZ and HAZ. Increasing the rotation rate from 400 to 800 rpm at a constant welding speed of 200 mm/min enhanced the hardness of the NZ and made the hardness distribution nonuniform but exerted no noticeable influence on the hardness of the HAZ. The location of LHZs was therefore located at the HAZ for sample 800–200. It should be noted that this result is different from that the hardness of LHZs was independent of rotation rate for the FSW joints of conventional precipitation–hardened aluminum alloys [10,21,22]. With further increasing the rotation rate from 800 to 1200 rpm at a constant welding speed of 200 mm/min, the hardness distribution was more uniform in the NZ, and the hardness of the LHZs obviously increased but the locations of the LHZs were unchanged.

Fig. 5b shows the effect of the welding speed on the hardness profiles of the FSW 2060–T8 joints. At a constant rotation rate of 1200 rpm, increasing the welding speed from 50 to 200 mm/min caused an obvious increase in the hardness of the LHZs but exerted almost no effect on the location of the LHZs and the hardness distribution of the NZ.

The above microhardness profiles indicate that the LHZs may be located at the NZ or the HAZ for the FSW 2060–T8 joints. Thus, the microstructure of the NZ and HAZ were particularly concerned in this study.

3.3. Precipitates

The Al–Cu–Li–Mg–Ag alloy in varied states may contain Guinier–Preston (GP) zones, Guinier–Preston–Bagaryatsky (GPB) zones, T_1, S′, δ′, β′, θ′ and σ precipitates [24,25]. The crystal structure and precipitation characteristics of these phases are summarized in Table 3 [26–37]. The identification of the precipitates in the matrix was conducted by means of the diffraction patterns according to three Al zone axes of [100], [110] and [112].

Fig. 6 schematizes the expected SAD patterns of the main precipitates in 2060 Al—Li alloys. It should be stressed that both δ′ and β′ precipitates have the similar LI_2 diffraction pattern and morphology, and they may form the composite precipitates of $Al_3(Li,Zr)$. Therefore, these LI_2 precipitates are not differentiated and referred to as δ′/β′ precipitates in this study. Because the NZ of sample 800–200 has the identical hardness with that of sample 1200–200 and the hardness of the HAZ of sample 800–200 is equivalent to that of sample 400–200, the precipitates of the NZ and the HAZ of samples 400–200, 1200–200 and 1200–50 were therefore examined in detail.

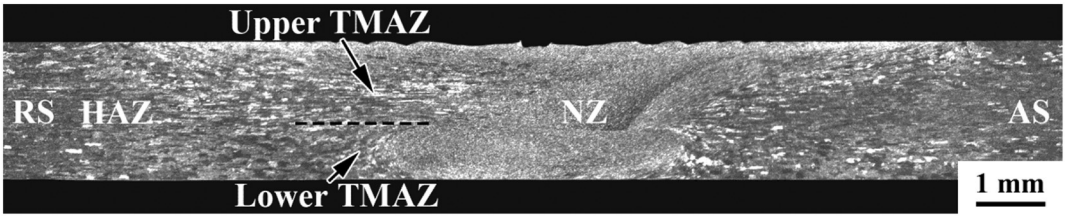

Fig. 2. Typical cross–sectional macrostructure of FSW 2060–T8 joint.

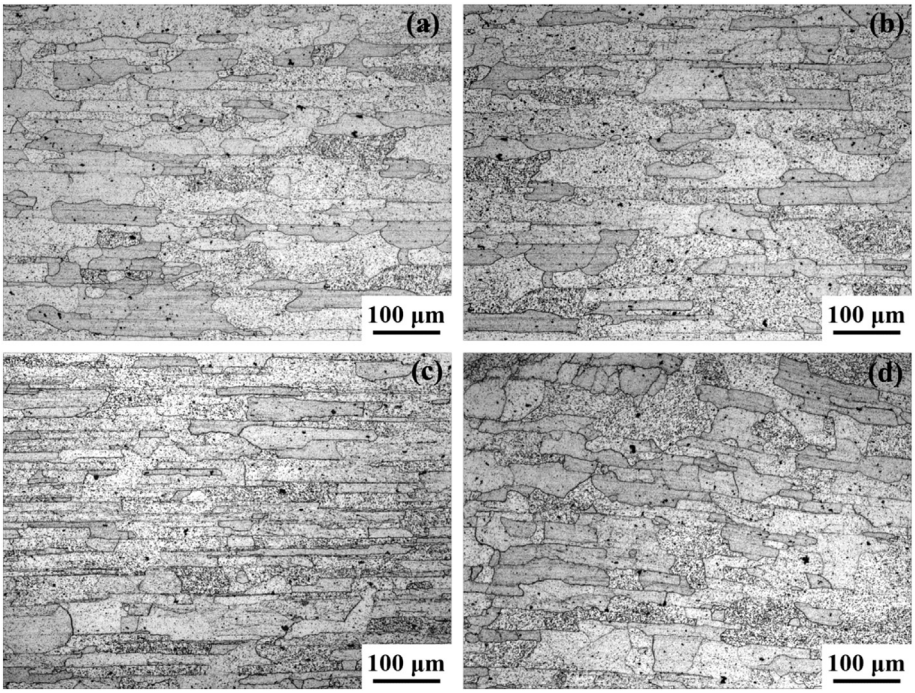

Fig. 3. Optical micrographs of sample 1200–200: (a) BM, (b) HAZ, (c) upper TMAZ and (d) lower TMAZ.

3.3.1. BM

Figs. 7 and 8 show the TEM bright field image, dark field image and SAD patterns of the BM. The incoherent rod–like precipitates with a typical size of 50–100 nm across and 500–800 nm in length (Fig. 7a) were identified as T ($Al_{20}Cu_2Mn_3$) precipitates by EDS analysis with the compositions of 10.1% (wt) Mn, 11.8% (wt) Cu, and the balance Al, which was in agreement with the results reported in Refs. [35] and [38]. The needle–like precipitates with a size of 46 nm in length in the high magnification bright field close to $\langle 110\rangle_{Al}$ of the BM was T_1 precipitates (Fig. 7b), which could be easily recognized in the SAD patterns, e.g., from the four symmetrically distributed spots at $1/3\langle 220\rangle_{Al}$ position in $\langle 100\rangle_{Al}$ zone axis (Fig. 8a), the two spots at $1/3\langle 220\rangle_{Al}$ position and streaks along $\langle 111\rangle_{Al}$ direction in the $\langle 110\rangle_{Al}$ zone axis (Fig. 8b) [11,30,39].

The tortuous precipitates near $\langle 100\rangle_{Al}$ zone axis of the BM were identified as S′ precipitates (Fig. 7c), which were evidenced by the faint streaks along $\langle 210\rangle_{Al}$ direction in the SAD patterns close to $\langle 112\rangle_{Al}$ zone axis (Fig. 8c) [28,40]. The S′ precipitates commonly showed lath–shaped but presented tortuous–shaped in 2060–T8 BM in this study. This is because S′ precipitates preferentially nucleated on dislocations during the T8 heat treatment [41,42]. Moreover, the superlattice spots at $1/2\langle 200\rangle_{Al}$ position in the SAD pattern close to $\langle 110\rangle_{Al}$

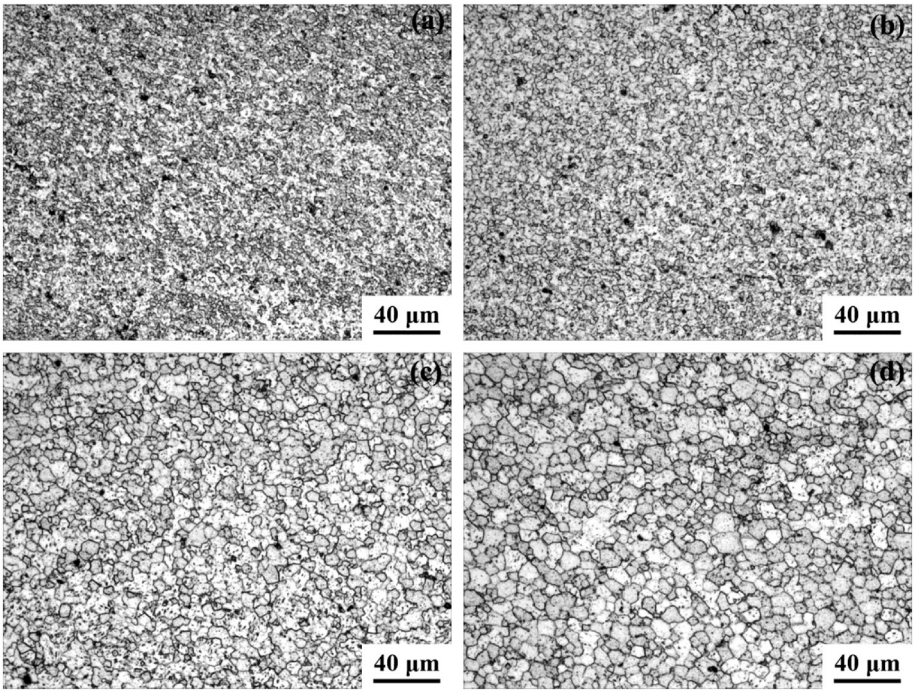

Fig. 4. Optical micrographs of NZ of samples (a) 400–200, (b) 800–200, (c) 1200–200 and (d) 1200–50.

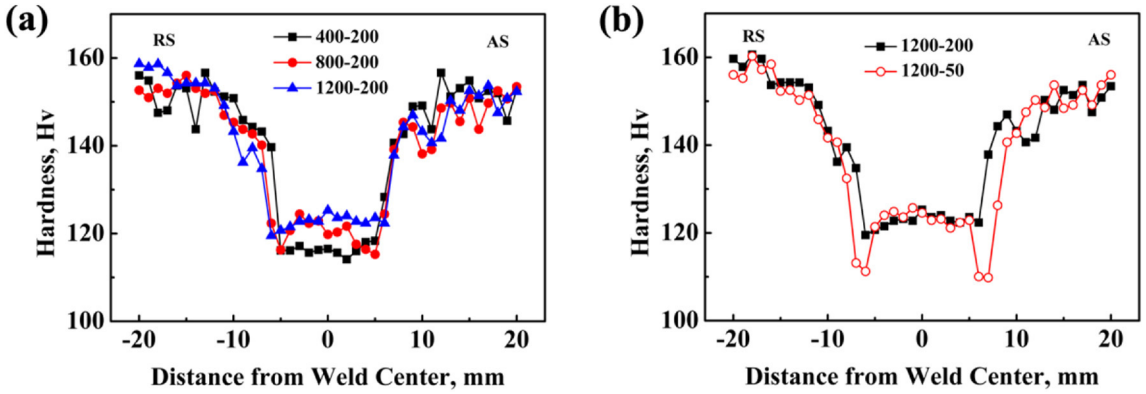

Fig. 5. Microhardness profiles of FSW 2060–T8 joints showing effect of (a) rotation rate and (b) welding speed.

Table 3
Crystal structure and precipitation characteristics of precipitates in Al–Li–Cu–Mg–Ag alloys.

Precipitate	Crystal structure	Morphology	Orientation	Reference
T	Orthorhombic	Rod–like		[26,27]
T_1	Hexagonal	Platelete (front view), needle–like (side view)	$(0001)\|\|(111)_{Al}$ $[10]\|\|[-110]_{Al}$	[28–30]
S′	Orthorhombic	Lath	$[100]\|\|[100]_{Al}$ $[010]\|\|[02-1]_{Al}$ $[001]\|\|[012]_{Al}$	[31–33]
δ′	$L1_2$	Spherical	$(111)\|\|(111)_{Al}$	[30,33]
β′	$L1_2$	Spherical	$(111)\|\|(111)_{Al}$	[33,34]
θ′	Tetragonal	Platelete (front view), needle–like (side view)	$[001]\|\|[100]_{Al}$	[30,35]
σ	Cubic	Cubical	$(100)\|\|(100)_{Al}$ $[100]\|\|[100]_{Al}$	[35–37]

zone axis in Fig. 8b revealed that the spherical precipitates in dark field micrograph were δ′/β′ precipitates (Fig. 7d). The above results show that T, T_1, S′ and δ′/β′ precipitates existed in the BM. This result is different from that reported in Refs. 17 and 18 where the main precipitates of 2060–T8 alloy were determined to be T, T_1, θ′ and S′ precipitates.

3.3.2. NZ

Fig. 9 shows the low magnification TEM bright field images of the NZ of samples 400–200, 1200–200 and 1200–50. It can be seen that the average size of equiaxed grains and rod-like or elliptical T precipitates in the NZ of sample 400–200 were about 2.0 μm and 100 nm, respectively, indicating that dynamic recrystallization and partial dissolution of T precipitates occurred (Fig. 9a). Increasing the rotation rate from 400 to 1200 rpm at a constant welding speed of 200 mm/min led to larger grain size and lower density of T precipitates in sample 1200–200 compared with that of sample 400–200 (Fig. 9b). Decreasing the welding speed from 200 to 50 mm/min at the rotation rate of 1200 rpm resulted in a larger grain size and almost complete dissolution of T precipitates in sample 1200–50 compared with that of sample 1200–200 (Fig. 9c).

Fig. 10 shows the high magnification TEM bright field images and associated SAD patterns of the NZ of samples 400–200, 1200–200 and 1200–50. Low density of spherical precipitates, most likely to be δ′/β′ precipitates judged by the morphology, were observed in the NZ of sample 400–200 (Fig. 10a), however, the SAD pattern showed only Al reflections (Fig. 10d). This is probably because the diffraction of the precipitates with a very low density was very weak and therefore hardly reflected in the SAD pattern.

Increasing the rotation rate from 400 to 1200 rpm at a constant welding speed of 200 mm/min led to a higher density of spherical precipitates in the NZ of sample 1200–200 (Fig. 10b). These precipitates produced superlattice spots at $1/2\langle 200\rangle_{Al}$ and $1/2\langle 220\rangle_{Al}$ positions in the $\langle 100\rangle_{Al}$ SAD patterns (Fig. 10e), indicating that they were δ′/β′ precipitates [28]. The GP and GPB zones were indiscernible under conventional TEM, but could be detected by the diffuse streaks along $\langle 100\rangle_{Al}$ direction. The diffuse streaks along $\langle 100\rangle_{Al}$ direction through the matrix Al reflections and diffuse streaks along $\langle 100\rangle_{Al}$ directions around $1/2\langle 220\rangle_{Al}$ position indicated the formation of GP and GPB zones [43–45] (Fig. 10e).

At a constant rotation rate of 1200 rpm, when decreasing the welding speed from 200 to 50 mm/min, the δ′/β′ precipitates, GP and GPB zones were essentially unchanged in the NZ of sample 1200–50 compared with that of sample 1200–200 (Fig. 10c and f).

3.3.3. HAZ

Fig. 11 shows the low magnification bright field images of the HAZ on the RS of samples 400–200, 1200–200 and 1200–50. For sample 400–200, the density of T precipitates in the HAZ was essentially unchanged and the size slightly decreased compared with that of the BM (Fig. 11a). The characteristics of T precipitates in the HAZ of sample 1200–200 were nearly identical to that of sample 400–200 (Fig. 11b). In contrast, the density and size of T precipitates remarkably decreased in the HAZ of sample 1200–50 compared to that of sample 1200–200 (Fig. 11c).

Figs. 12 and 13 show the high magnification bright field images and SAD patterns, respectively, of the HAZ close to $\langle 110\rangle_{Al}$ and $\langle 100\rangle_{Al}$ zone axes for samples 400–200, 1200–200 and 1200–50. For the HAZ of sample 400–200, T_1 and S′ precipitates were coarsened and exhibited an obvious decrease in density as compared with those in the BM (Fig. 12a and d). The coarsened and lath–like precipitates lying along $\langle 200\rangle_{Al}$ direction were θ′ precipitates, which were confirmed by the streaks with maximum intensity along $\langle 100\rangle_{Al}$ direction in the $\langle 100\rangle_{Al}$ SAD patterns [39,44] (Fig. 13a). Moreover, the cubic precipitates produced symmetrically distributed spots at $1/4\langle 200\rangle_{Al}$ and $1/4\langle 220\rangle_{Al}$ positions in the $\langle 110\rangle_{Al}$ SAD patterns (Fig. 13b), and were therefore identified as σ precipitates [32] (Fig. 12a and d). It is noted that θ′ and σ precipitates were not found in the BM but were observed in the HAZ of FSW 2060–T8 joints in this study.

For sample 1200–200, the density and size of T_1 precipitates were essentially unchanged but the density of S′, θ′ and σ precipitates increased in the HAZ compared with that for sample 400–200 (Figs. 12b, e, and 13d–f). However, for sample 1200–50, the T_1, S′, θ′ and σ precipitates were coarser, and the density of T_1, S′, and σ precipitates decreased, while the density of θ′ precipitates increased compared with that for sample 1200–200 (Figs. 12c, f, and 13g–i).

3.4. Tensile strength

The UTS and failure locations of the FSW 2060–T8 joints are shown

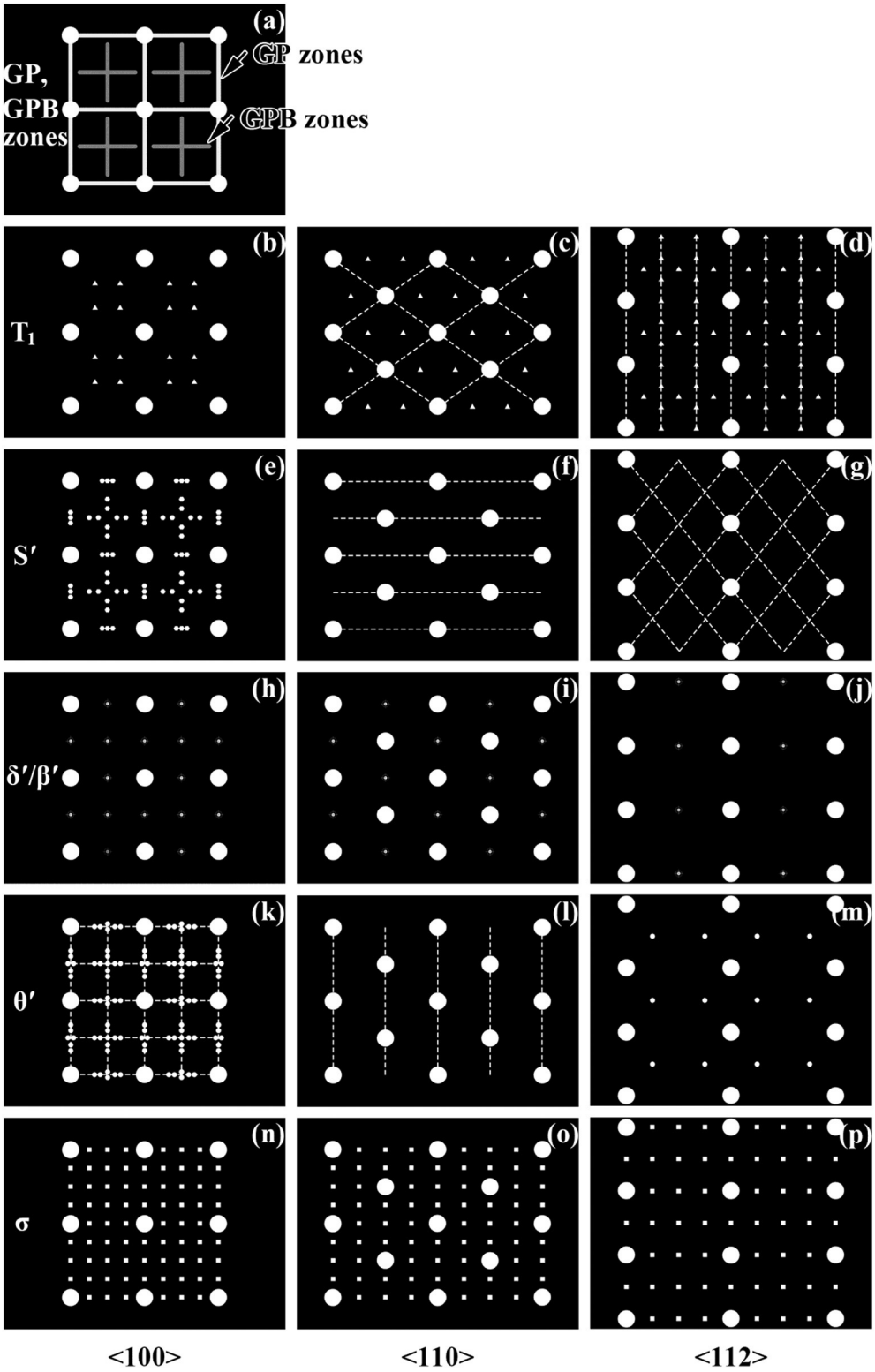

Fig. 6. Scheme of SAD patterns of main precipitates of 2060–T8 alloy in three main zone axes: (a) ⟨100⟩ of GP and GPB zones; (b) ⟨100⟩, (c) ⟨110⟩ and (d) ⟨112⟩ of T_1 precipitate; (e) ⟨100⟩, (f) ⟨110⟩ and (g) ⟨112⟩ of S′ precipitate; (h) ⟨100⟩, (i) ⟨110⟩ and (g) ⟨112⟩ of δ′/β′ precipitate; (k) ⟨100⟩, (l) ⟨110⟩ and (m) ⟨112⟩ of θ′ precipitate; (n) ⟨100⟩, (o) ⟨110⟩ and (p) ⟨112⟩ of σ precipitate.

in Table 4. Table 4 reveals three important findings. Firstly, under a constant welding speed of 200 mm/min, increasing the rotation rate from 400 to 800 rpm improved the UTS of the FSW 2060–T8 joints. However, the UTS was essentially unchanged when further increasing the rotation rate from 800 to 1200 rpm. Secondly, under a constant rotation rate of 1200 rpm, increasing the welding speed from 50 to 200 mm/min obviously increased the UTS of the FSW 2060–T8 joints. Thirdly, for the FSW 2060–T8 joints, the failure locations were normally at the LHZs under 400 rpm–200 mm/min and 1200 rpm–50 mm/min, but the abnormal failure occurred at the TMAZ under

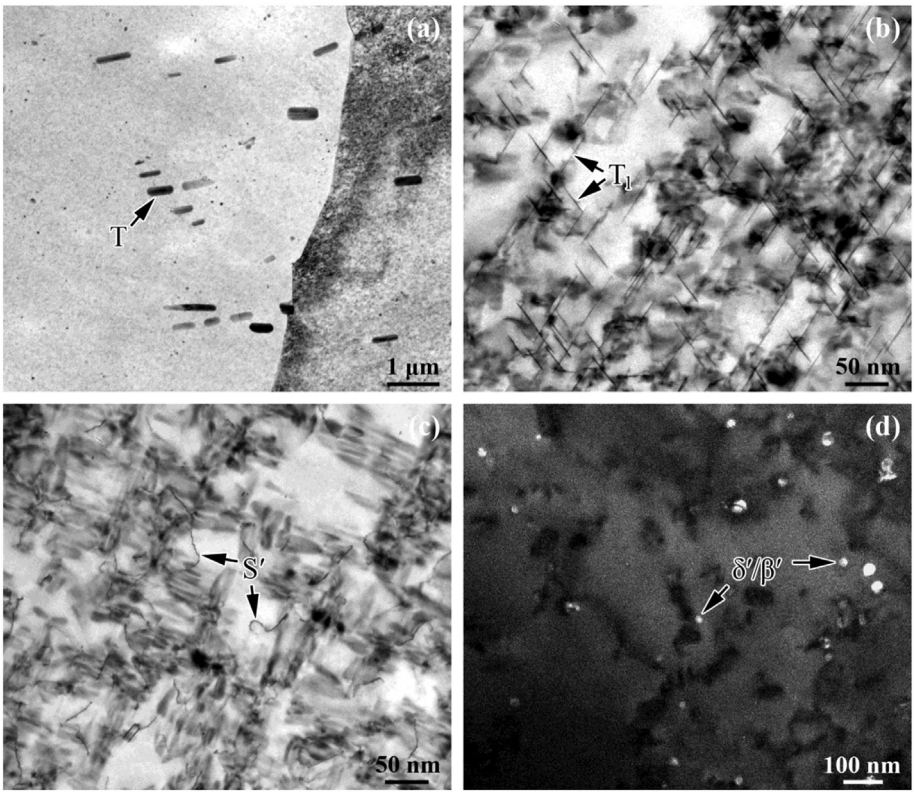

Fig. 7. TEM micrographs of 2060–T8 BM: (a) low magnified bright field; high magnified BF along (b) $\langle 110\rangle_{Al}$, (c) $\langle 100\rangle_{Al}$ zone axes, and (d) dark field.

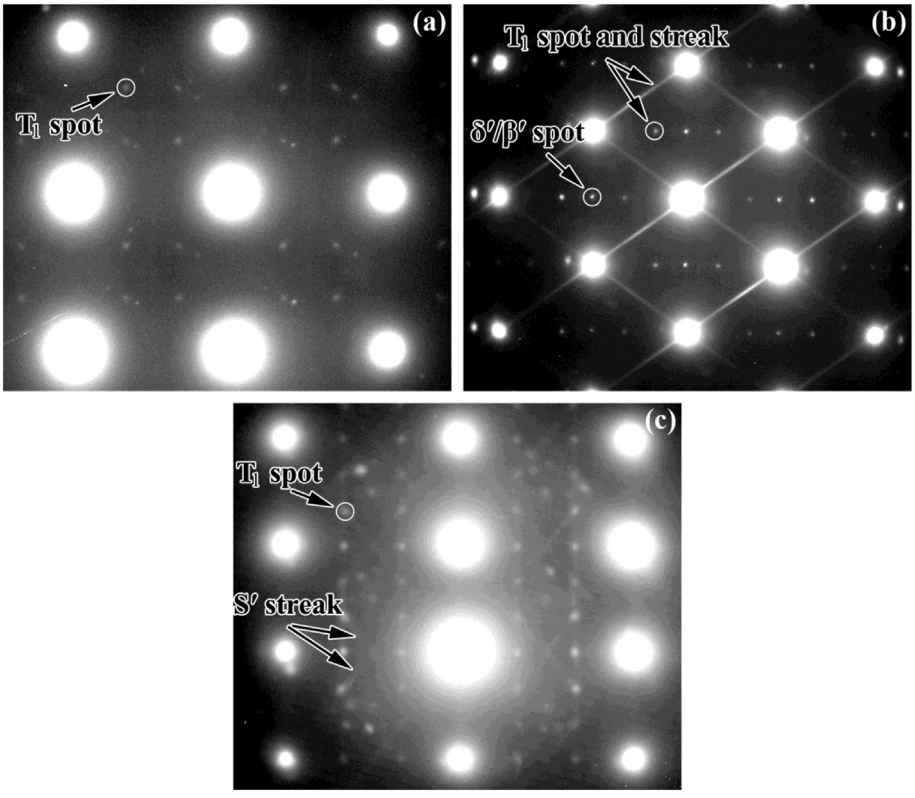

Fig. 8. TEM SAD patterns of 2060–T8 BM: (a) $\langle 100\rangle_{Al}$, (b) $\langle 110\rangle_{Al}$ and (c) $\langle 112\rangle_{Al}$ zone axes.

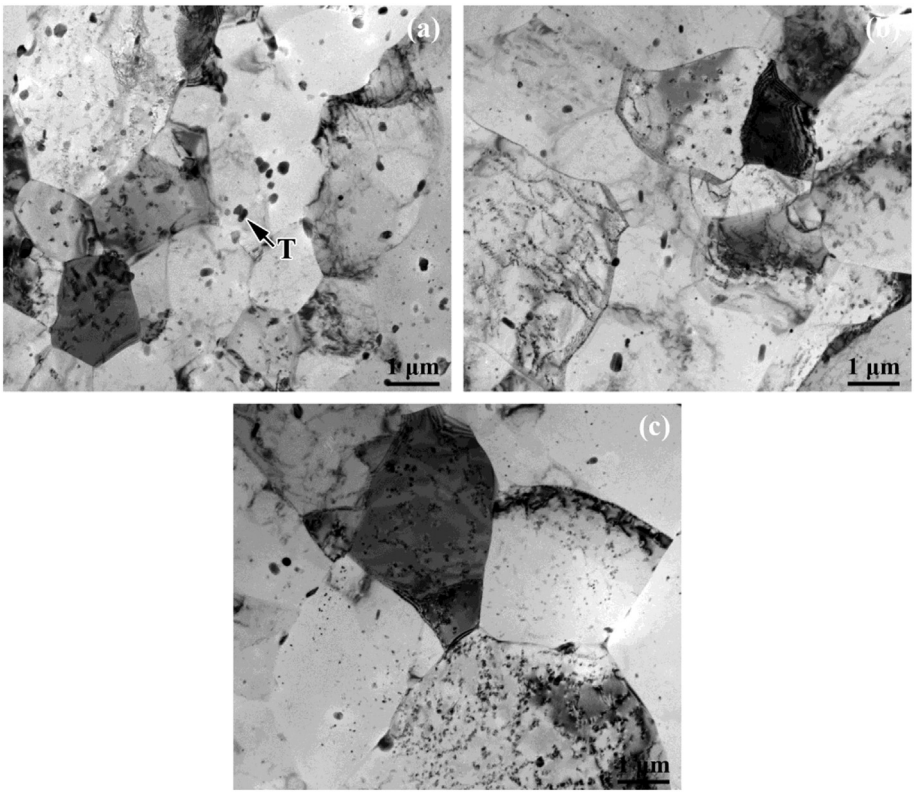

Fig. 9. Low magnification TEM bright field micrographs of NZ of FSW 2060–T8 joints: (a) 400–200, (b) 1200–200 and (c) 1200–50.

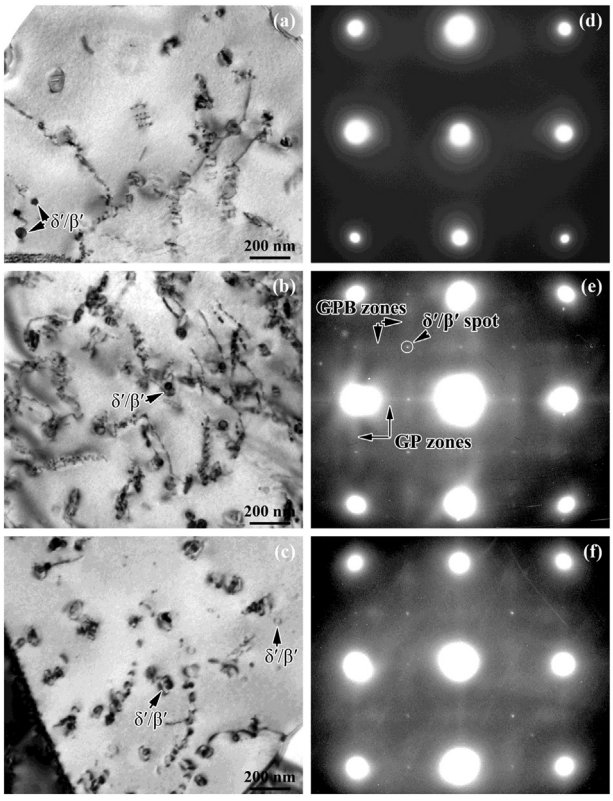

Fig. 10. High magnified TEM bright field of NZ of FSW 2060–T8 joints: (a) 400–200, (b) 1200–200, and (c) 1200–50; TEM SAD patterns in ⟨100⟩ zone axis of NZ of FSW 2060–T8 joints: (d) 400–200, (e) 1200–200, and (f) 1200–50.

800 rpm–200 mm/min and 1200 rpm–200 mm/min.

4. Discussion

4.1. Precipitates in 2060–T8 alloy

The 2060Al alloy is a multicomponent Al–Cu–Li–Mg–Ag alloy and has a certain natural aging tendency. The general precipitation sequence (PS) of Al–Cu–Li alloy from the supersaturated solid solution (SSSS) during artificial aging was dependent on Cu/Li ratio [46]:

$$\mathrm{Cu/Li} > 5,\ \mathrm{SSSS} \rightarrow \mathrm{GP/GPB\ zones} + \delta' \rightarrow \delta' + \theta'' \rightarrow \delta' + \theta' \rightarrow \delta + \theta \quad (1)$$

$$5 > \mathrm{Cu/Li} > 2,\ \mathrm{SSSS} \rightarrow \mathrm{GP/GPB\ zones} + \delta' \rightarrow T_1 + \delta' \rightarrow T_1 \quad (2)$$

$$\mathrm{Cu/Li} < 2,\ \mathrm{SSSS} \rightarrow \delta' \rightarrow T_1 + \delta' \quad (3)$$

The theoretical Cu/Li ratio of 2060 Al alloy is 5.37 in this study. According to PS (1), θ′ precipitate should exist in the 2060–T8 alloy. However, no θ′ precipitate was observed in the BM in this study (Fig. 7b and c). There are two possible reasons: (1) θ′ precipitates existed hardly in the BM and therefore were not detected by TEM; (2) the formation of S′ precipitates consumed Cu element, led to the decrease of the Cu/Li ratio in local regions. The original T_1, S′ and δ′/β′ precipitates in the BM formed during T8 artificial aging at 190 °C, while T precipitate usually formed in the ingot homogenization process and exhibited better thermal stability compared to other precipitates during the subsequent solution and aging treatment [35]. δ′ precipitate would dissolve at 230 °C, whereas T_1, S′ and θ′ precipitates would coarsen at 300–400 °C and dissolve at 450–500 °C [47,48].

4.2. Microstructure and hardness evolution of FSW 2060–T8 joints

The precipitate evolution in the FSW 2060–T8 joints are summarized in Table 5. During FSW, the various positions of the FSW joints

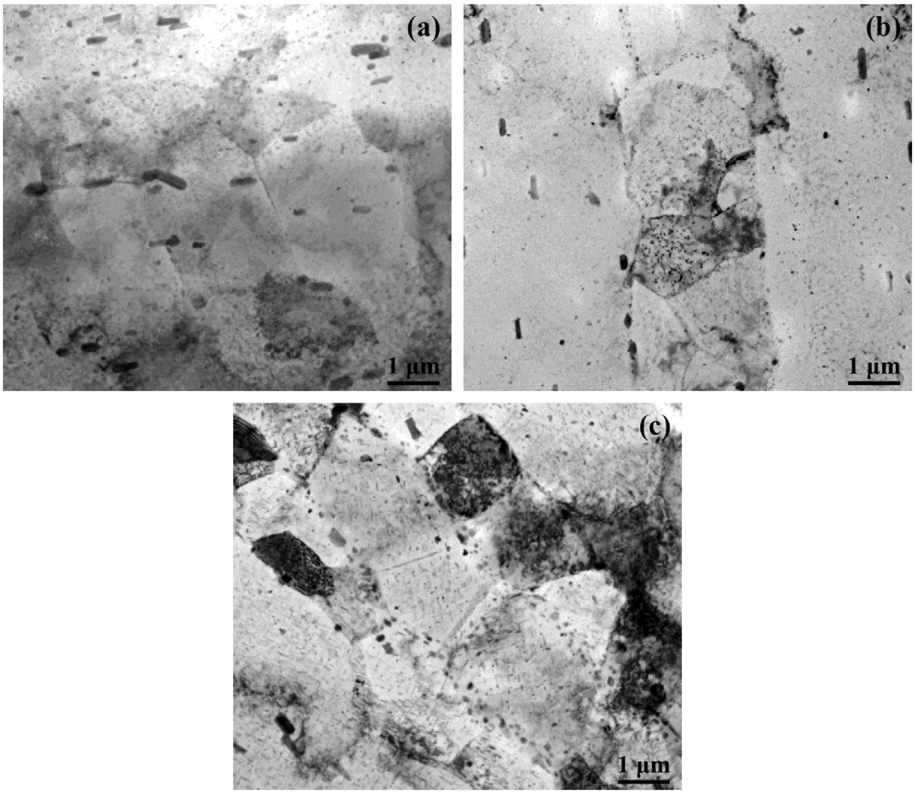

Fig. 11. Low magnified TEM of HAZ of FSW 2060–T8 joints: (a) 400–200, (b) 1200–200 and (c) 1200–50.

experienced different thermal cycles. The precipitates therefore evolved in different ways at the various positions. Based on the correlation between the precipitate evolution and the hardness distribution, two sub–zones can be named on the transverse cross–section of the FSW 2060–T8 joint, i.e., dissolution zone and overaging zone. Generally, the dissolution zone corresponds to the NZ while the overaging zone contained the TMAZ and the HAZ [9,10].

4.2.1. Microstructure evolution and hardness distribution in NZ

Generally, for most of the precipitation–hardened Al—Li alloys, the dissolution zone was located at the NZ, which experienced severe plastic deformation and high heat input with the peak temperature of about 400–500 °C during FSW [10,49], leading to the formation of the supersaturated solid solution in the NZ. Thus, only δ′ precipitate, GP zones or GPB zones formed in the NZ of FSW Al—Li joints during the subsequent natural aging process. For sample 400–200, FSW resulted in the complete dissolution of the T_1, S′, δ′ precipitates, partial dissolution of the T precipitate, as well as the reprecipitation of δ′ precipitate in the NZ (Figs. 9a, 10a and d). Increasing the rotation rate from 400 to 800 and 1200 rpm under the welding speed of 200 mm/min resulted in higher peak temperature and severer plastic deformation, causing the severer dissolution of T precipitates, the higher density of δ′ precipitates, as well as the formation of GP and GPB zones in the NZ (Figs. 9b, 10b and e). Thus, the NZ of sample 1200–200 exhibited higher hardness compared with that of sample 400–200 (Fig. 5a). The reason that GP and GPB zones formed in the NZ of sample 1200–200 rather than that of sample 400–200 can be elucidated as follows.

The FSW heat input and plastic deformation are related with the rotation rate/welding speed ratio. The heat input and plastic deformation at 400 rpm–200 mm/min was not high enough to produce the sufficient vacancies and adequate supersaturation of alloying elements, which strongly slowed down the formation of GP and GPB zones at room temperature after welding. Increasing the rotation rate from 400 to 800 and 1200 rpm under a constant welding speed of 200 mm/min resulted in higher peak temperature and severer plastic deformation, which was conducive to produce the sufficient vacancies, accelerated the dissolution of T precipitates. This eventually benefited the supersaturation of alloying elements and facilitated the formation of the GP and GPB zones.

The welding parameters of 1200 rpm–200 mm/min provided adequate heat input for precipitate dissolution for the NZ. In this case, as the welding speed decreased from 200 to 50 mm/min at a constant rotation rate of 1200 rpm, although the dissolution duration (duration above the precipitate dissolution temperature) increased, the precipitates in the NZ of sample 1200–50 were nearly identical to that of sample 1200–200 (Figs. 9c, 10c and f). Thus, sample 1200–50 exhibited almost the identical hardness profile at the NZ with sample 1200–200 (Fig. 5b).

4.2.2. Microstructure evolution and hardness softening mechanism in HAZ

The overaging zone of FSW precipitation–hardened aluminum alloys corresponds to the TMAZ and HAZ. The peak temperatures of the thermal cycles at this zone were considered to be between 200 and 400 °C [11,50]. In particular, it was reported that most of the LHZs were located at the HAZ and experienced thermal cycles with the same peak temperature of 360–370 °C, 340 °C and 300–340 °C for FSW 6061Al–T6 joints [21], FSW 2024Al–T351 joints [10] and FSW 2098Al–T351 joints [49], respectively. Thus, it could be conjectured that the HAZ of the FSW 2060–T8 joints also experienced similar thermal cycles, resulting in the different degrees of dissolution and coarsening of T, T_1 and S′ precipitates, dissolution of δ′/β′ precipitates and formation of σ and θ′ precipitates (Figs. 11 and 12).

However, different from the result that the precipitates were coarsened and dissolved in the HAZ for FSW joints of conventional precipitation–hardened aluminum alloys, both σ and θ′ precipitates were absent in the BM but were formed in the HAZ for FSW 2060–T8 joints in this study (Fig. 12). Schueller et al. [51] reported that in an Al–4.3Cu–2.0 Mg (wt%) alloy with Si addition, formation of Si clusters

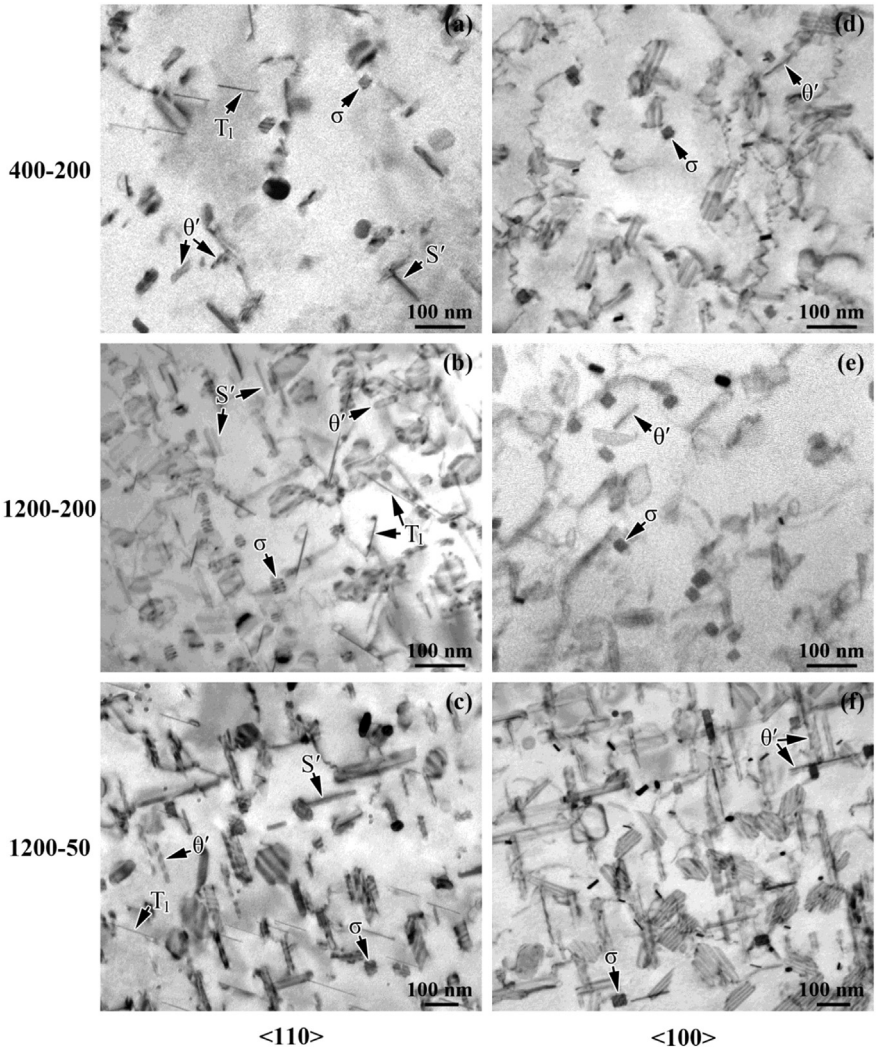

Fig. 12. High magnified TEM images of HAZ of FSW 2060–T8 joints: (a) and (d) along $\langle 110\rangle_{Al}$ and $\langle 100\rangle_{Al}$ of sample 400–200; (b) and (e) along $\langle 110\rangle_{Al}$ and $\langle 100\rangle_{Al}$ of sample 1200–200; (c) and (f) along $\langle 110\rangle_{Al}$ and (f) $\langle 100\rangle_{Al}$ of sample 1200–50.

generated a compressive strain in the matrix which attracted a high concentration of Cu atoms to their interface, and then σ precipitates nucleated in this high–Cu region. Li et al. [32] pointed out that a high concentration of Cu was required in a local zone for nucleation of σ precipitates. In the present study, the substantial dissolution of T_1, S′ and T precipitates allowed release of sufficient amounts of Cu into the matrix in the HAZ and therefore provided an excellent condition for nucleation of σ precipitates (Fig. 12). θ′ precipitates was believed to nucleate in Cu rich region on condition that Mg is insufficient for σ precipitate formation in the HAZ of FSW 2060–T8 joints.

The coarsening degree and hardness of the HAZ was dependent on the duration above the aging temperature; i.e., over–aging time, which was related to the welding speed and independent of the rotation rate for the FSW conventional precipitation–hardened aluminum alloys [9,10,20]. During FSW, the precipitates partially dissolved in the HAZ and the solute clusters would be formed after post–welding natural aging [10]. In this study, sample 400–200 exhibited lower natural aging tendency due to lack of vacancies compared with that of sample 1200–200. Thus, sample 400–200 exhibited the lower precipitate density and hardness in the HAZ compared with sample 1200–200 (Figs. 5a, 10a and d), though samples 400–200 and 1200–200 had the same over–aging time in this study.

Increasing the welding speed would decrease the over–aging duration of the precipitates, and vice versa. Sample 1200–200 experienced a shorter over–aging time than sample 1200–50, indicating slighter dissolution and coarsening of precipitates in the HAZ of sample 1200–200 than that of sample 1200–50 (Fig. 12b, c, e and f). Thus, the hardness of the LHZs of the FSW 2060–T8 joints increased when increasing the welding speed from 50 to 200 mm/min under a constant rotation rate of 1200 rpm (Fig. 5b).

4.3. Tensile strength and failure locations of FSW 2060–T8 joints

The variation of the tensile strength and the abnormal failure locations of FSW joints of 2060–T8 and conventional precipitation–hardened aluminum alloys are summarized in Table 6. It revealed that, compared with that of FSW joints of 2060–T8 in Refs. 17–19 and conventional precipitation–hardened aluminum alloys, the UTS and failure locations showed the distinctly different characteristics for the FSW 2060–T8 joints in this study.

Firstly, the joint strength first markedly increased and then remained unchanged with increasing the rotation rate, and was improved with increasing the welding speed for the FSW 2060–T8 joints in this study (Table 6). However, in previous studies [17–19], with increasing the rotation rate or welding speed, the UTS of the FSW 2060–T8 joints first increased and then decreased. Moreover, the abnormal failure location was located at the TMAZ in this study, but the FSW joints abnormally fractured at the NZ or NZ/TMAZ interface in the previous

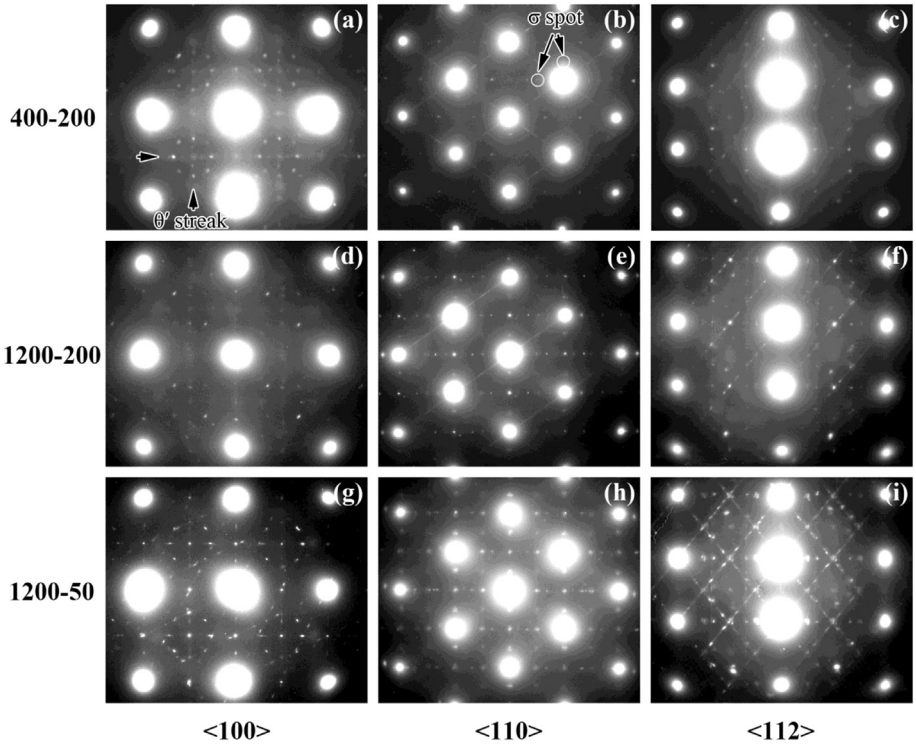

Fig. 13. TEM SAD patterns of HAZ of FSW 2060–T8 joints: (a) $\langle 100\rangle_{Al}$, (b) $\langle 110\rangle_{Al}$ and (c) $\langle 112\rangle_{Al}$ zone axes of sample 400–200; (d) $\langle 100\rangle_{Al}$, (e) $\langle 110\rangle_{Al}$ and (f) $\langle 112\rangle_{Al}$ zone axes of sample 1200–200; (g) $\langle 100\rangle_{Al}$, (h) $\langle 110\rangle_{Al}$ and (i) $\langle 112\rangle_{Al}$ zone axes of sample 1200–50.

Table 4
Transverse tensile properties of FSW 2060–T8 joints.

Welding parameter (rpm–mm/min)	UTS (MPa)	El. (%)	Fracture location
BM	528.1 ± 2.5	15.6 ± 0.6	–
400–200	413.6 ± 0.4	9.2 ± 0.0	NZ
800–200	446.5 ± 1.9	11.6 ± 0.4	TMAZ
1200–200	444.8 ± 0.7	12.5 ± 0.5	TMAZ
1200–50	423.5 ± 3.2	9.7 ± 0.8	HAZ

studies [17–19]. Considering the fact that the joint surface thinning might exert significant effect on the mechanical properties and fracture locations of FSW joints of thin plates in the previous studies [17–19], the present results based on the joint surface planing exactly reflects the intrinsic UTS and abnormal fracture behavior.

Secondly, for the FSW joints of conventional precipitation–hardened aluminum alloys, the UTS of the FSW joints increased with increasing the welding speed and was independent of rotation rate because the LHZs determined the mechanical properties of the FSW joints [21,22]. For the FSW 2060–T8 joints in this study, while the welding speed exerted the identical effect on the intrinsic UTS, the effect of the rotation rates on the joint strength and failure locations were different from that for the FSW joints of conventional precipitation–hardened aluminum alloys, which could not be explained by the hardness distribution. This indicates that there are other factors affecting the intrinsic UTS and failure locations of the FSW 2060–T8 joints except for the joint

Table 6
Variation of tensile strength with welding parameters and abnormal failure locations of FSW joints of 2 mm thick 2060–T8 in Refs. 17–19 and this study, and conventional precipitation–hardened (CPH) aluminum alloys.

Alloys	UTS variation		Abnormal failure locations	Refs.
	Increasing rotation rate	Increasing welding speed		
CPH Al	→	↗	–	[9,10,21,22]
2060–T8	First ↗ and then ↘	First ↗ and then ↘	NZ or NZ/TMAZ	[17–19]
2060–T8	First ↗ and then →	↗	TMAZ	This study

→: Unchange; ↗: Increase; ↘: Decrease.

Table 5
Summary of precipitates in various zones of FSW 2060–T8 joints.

Welding parameter	Region	Precipitates evolution
–	BM	T, T_1, S′ and δ′/β′
400–200	NZ	T_1, S′ and δ′/β′ completely dissolved; T partially dissolved; δ′/β′ reprecipitated;
	HAZ	Dissolved dominantly: (1) T partially dissolved; (2) θ′ and σ formed and coarsened; (3) T_1 and S′ density ↘, size ↗;
1200–200	NZ	T, T_1, S′, and δ′/β′ completely dissolved; δ′/β′, GP and GPB zones reprecipitated;
	HAZ	Dissolved and coarsened dominantly: (1) T partially dissolved; (2) T_1 density →, size ↗; (3) S′, θ′ and σ: density ↗, size →;
1200–50	NZ	T, T_1, S′, and δ′/β′ completely dissolved; δ′/β′, GP and GPB zones reprecipitated;
	HAZ	Coarsened dominantly: (1)T further dissolved; (2) T_1, S′ and σ: density ↘, size ↗; (3) θ′: size and density ↗;

→: Unchange; ↗: Increase; ↘: Decrease.

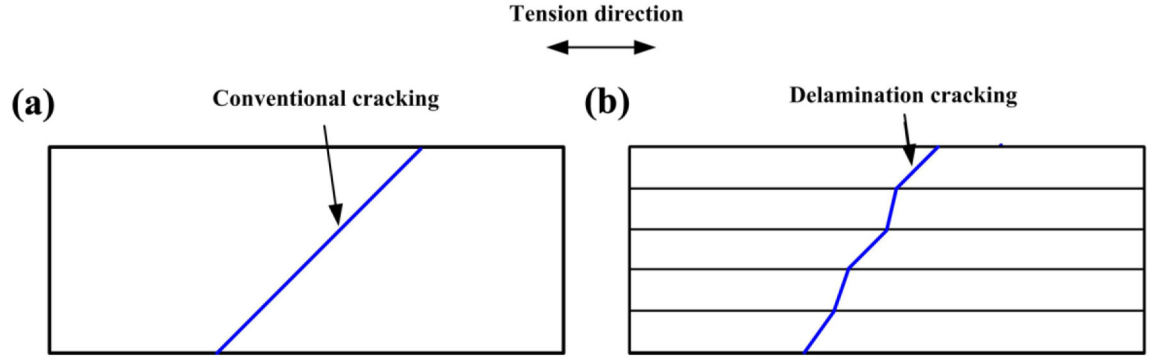

Fig. 14. Tension failure schematic diagram of (a) the cracking for conventional precipitation–hardened aluminum alloys and (b) delamination cracking for Al—Li alloys.

surface thinning and the hardness distribution.

One factor that influenced the intrinsic UTS of the FSW 2060–T8 joints is related with the delamination cracking. It was reported that the delamination cracking along elongated grain boundaries was a common phenomenon in Al—Li alloys [52–55], leading to significant anisotropy of tensile, fatigue, and failure properties [52,53]. When the primary macrocrack propagation orientation was perpendicular to the delamination plane during tension, the delamination cracking acted as the "crack arrester" or "crack divider" for the primary macrocrack [55], inhibiting the propagation of the primary macrocrack. That is to say, different from the fracture mode of the conventional precipitation–hardened aluminum alloys that primary macrocrack generated at one point and then crossed the specimens (Fig. 14a), the rolled Al—Li alloys exhibited multiple delamination cracking phenomena along the thin and long grains during tension, and the primary macrocrack might generate separately for per delamination (Fig. 14b). This means that the delamination cracking could strengthen the upper TMAZ and HAZ with elongated grains for the FSW 2060–T8 joints. Therefore, the strength of the FSW 2060–T8 joints was enhanced by the delamination cracking. The delamination cracking in the BM and sample 1200–50 will be shown and discussed in detail in the companion paper.

As a result, the intrinsic UTS was improved with increasing the rotation rates from 400 to 800 rpm at a constant welding speed of 200 mm/min (Table 4), although sample 800–200 presented the similar hardness at the LHZs (HAZs) compared to sample 400–200 at the LHZ (NZ). For the same reason, the UTS of sample 1200–50 was higher than that of sample 400–200 (Table 4), although the hardness of sample 1200–50 at the LHZs (HAZs) was lower than that of sample 400–200 at the LHZ (NZ).

The other factor that influenced the intrinsic UTS of the FSW 2060–T8 joints is related with the abnormal fracture behavior. The LHZ of sample 1200–200 exhibited a higher hardness compared with that of sample 800–200 in this study, however the intrinsic UTS of the FSW 2060–T8 joints was essentially unchanged with increasing the rotation rate from 800 to 1200 rpm at a constant welding speed of 200 mm/min. This is attributed to that both of samples 800–200 and 1200–200 abnormally fractured at the TMAZ with the nearly identical hardness, instead of the HAZ where the hardness gap is large, resulting in the similar joint strength for samples 800–200 and 1200–200. The reasons for the abnormal fracture phenomena will be detailedly elaborated in the companion paper.

5. Conclusions

(1) Most of the T, T_1, S′ and δ′/β′ precipitates were dissolved in the NZ of the FSW 2060–T8 joints. δ′/β′ precipitates re–precipitated in the NZ under 400 rpm–200 mm/min, whereas both δ′/β′ precipitates, GP and GPB zones formed in the NZ under rotation rates of 800–1200 rpm and welding speeds of 50–200 mm/min.
(2) FSW thermal cycle resulted in the dissolution of T, T_1, S′ and δ′/β′ precipitates, coarsening of T_1 and S′ precipitates, as well as formation of σ and θ′ precipitates in the HAZ of FSW 2060–T8 joints.
(3) The LHZs of the FSW 2060–T8 joints were located at the NZ under 400 rpm–200 mm/min, but were located at the HAZ under rotation rates of 800–1200 rpm and welding speeds of 50–200 mm/min.
(4) The ultimate tensile strength of FSW 2060–T8 joints increased as the rotation rate increased from 400 to 800 rpm, but was unchanged with further increasing the rotation rate from 800 to 1200 rpm under a constant welding speed of 200 mm/min. And the joint strength increased as the welding speed increased from 50 to 200 mm/min under a constant rotation rate of 1200 rpm.
(5) The FSW 2060–T8 joints normally fractured at the LHZs under 400 rpm–200 mm/min and 1200 rpm–50 mm/min, but the abnormal failure occurred at the non–LHZ TMAZ under 800 rpm–200 mm/min and 1200 rpm–200 mm/min.

Data availability

The raw/processed data required to reproduce these findings cannot be shared at this time as the data also forms part of an ongoing study.

Declaration of competing interest

The authors declare that they have no known competing financial interests or personal relationships that could have appeared to influence the work reported in this paper.

Acknowledgements

The authors gratefully acknowledge the support of the National Natural Science Foundation of China (No. U1760201).

References

[1] Q. Chua, W.Y. Li, X.W. Yang, J.J. Shen, A. Vairisa, W.Y. Feng, W.B. Wang, Microstructure and mechanical optimization of probeless friction stir spot welded joint of an Al–Li alloy, J. Mater. Sci. Technol. 34 (2018) 1739–1746, https://doi.org/10.1016/j.jmst.2018.03.009.
[2] J. Zhang, X.S. Feng, J.S. Gao, H. Huang, Z.Q. Ma, L.J. Guo, Effects of welding parameters and post–heat treatment on mechanical properties of friction stir welded AA2195–T8 Al–Li alloy, J. Mater. Sci. Technol. 34 (2018) 219–227, https://doi.org/10.1016/j.jmst.2017.11.033.
[3] G.Q. Chen, Q.X. Yin, G. Zhang, B.G. Zhang, Fusion–diffusion electron beam welding of aluminum–lithium alloy with Cu nano–coating, Mater. Des. 188 (2020) 108439, , https://doi.org/10.1016/j.matdes.2019.108439.
[4] R.S. Mishra, Z.Y. Ma, Friction stir welding and processing, Mater. Sci. Eng. R 50 (2005) 1–78, https://doi.org/10.1016/j.mser.2005.07.001.
[5] Y. Chen, H. Wang, X.Y. Wang, H. Ding, J.W. Zhao, F.H. Zhang, Z.H. Ren, Influence of tool pin eccentricity on microstructural evolution and mechanical properties of friction stir processed Al–5052 alloy, Mater. Sci. Eng. A 739 (2019) 272–276, https://doi.org/10.1016/j.msea.2018.10.057.

[6] D. Chen, J.L. Li, H.X. Zhao, Z.J. Tan, J.T. Xiong, Effect of submillimeter variation in plunge depth on microstructure and mechanical properties of FSLW 2A12 aluminum alloy joints, Acta Metal. Sin. (Eng. Lett.) 33 (2020) 1165–1171, https://doi.org/10.1007/s40195-019-00981-5.

[7] G.Q. Chen, S. Zhang, Y.C. Zhu, C.L. Yang, Q.Y. Shi, Thermo-mechanical analysis of friction stir welding: a review on recent advances, Acta Metal. Sin. (Eng. Lett.) 33 (2020) 3–12, https://doi.org/10.1007/s40195-019-00942-y.

[8] Y. Du, T. Mukherjee, T. DebRoy, Conditions for void formation in friction stir welding from machine learning, Comp. Mater. 5 (2019) 68–75, https://doi.org/10.1038/s41524-019-0207-y.

[9] Z. Zhang, B.L. Xiao, Z.Y. Ma, Enhancing mechanical properties of friction stir welded 2219Al–T6 joints at high welding speed through water cooling and post-welding artificial ageing, Mater. Charact. 106 (2015) 255–265, https://doi.org/10.1016/j.matchar.2015.06.003.

[10] Z. Zhang, B.L. Xiao, Z.Y. Ma, Hardness recovery mechanism in the heat–affected zone during long–term natural aging and its influence on the mechanical properties and fracture behavior of friction stir welded 2024Al–T351 joints, Acta Mater. 73 (2014) 227–239, https://doi.org/10.1016/j.actamat.2014.04.021.

[11] A.K. Shukla, W.A. Baeslack, Study of microstructural evolution in friction–stir welded thin–sheet Al–Cu–Li alloy using transmission–electron microscopy, Scr. Mater. 56 (2007) 513–516, https://doi.org/10.1016/j.scriptamat.2006.11.028.

[12] A.K. Shukla, W.A. Baeslack, Study of process/structure/property relationships in friction stir welded thin sheet Al–Cu–Li alloy, Sci. Technol. Weld. Joi. 14 (2009) 376–387, https://doi.org/10.1179/136217109X412409.

[13] P. Cavaliere, M. Cabibbo, F. Panella, A. Squillace, 2198 Al–Li plates joined by friction stir welding: mechanical and microstructural behavior, Mater. Des. 30 (2009) 3622–3631, https://doi.org/10.1016/j.matdes.2009.02.021.

[14] C. Gao, Z.X. Zhu, J. Han, H.J. Li, Correlation of microstructure and mechanical properties in friction stir welded 2198–T8 Al–Li alloy, Mater. Sci. and Eng A 639 (2015) 489–499, https://doi.org/10.1016/j.msea.2015.05.038.

[15] A. Steuwer, M. Dumont, J. Altenkirch, S. Birosca, A. Deschamps, P.B. Prangnell, P.J. Withers, A combined approach to microstructure mapping of an Al–Li AA2199 friction stir weld, Acta Mater. 59 (2011) 3002–3011, https://doi.org/10.1016/j.actamat.2011.01.040.

[16] F. De Geuser, B. Malard, A. Deschamps, Microstructure mapping of a friction stir welded AA2050 Al–Li–Cu in the T8 state, Philos. Mag. 94 (2014) 1451–1462, https://doi.org/10.1080/14786435.2014.887862.

[17] Y.Q. Mao, L.M. Ke, F.C. Liu, C.P. Huang, Y.H. Chen, Q. Liu, Effect of welding parameters on microstructure and mechanical properties of friction stir welded joints of 2060 aluminum lithium alloy, Inter. J. Adv. 81 (2015) 1419–1431, https://doi.org/10.1007/s00170-015-7191-2.

[18] K. Yan, T.Y. Wang, H.M. Liang, Y. Zhao, Effects of rotation speed on microstructure and mechanical properties of 2060 Al–Cu–Li alloy in friction stir welding, Mater. Eng. Perform. 27 (2018) 5803–5814, https://doi.org/10.1007/s11665-018-3650-x.

[19] H.J. Liu, Y.J. Hu, C. Dou, D.P. Sekulic, An effect of the rotation speed on microstructure and mechanical properties of the friction stir welded 2060–T8 Al–Li alloy, Mater. Charact. 123 (2017) 9–19, https://doi.org/10.1016/j.matchar.2016.11.011.

[20] B. Cai, Z.Q. Zheng, D.Q. He, S.C. Li, H.P. Li, Friction stir weld of 2060 Al–Cu–Li alloy: microstructure and mechanical properties, J. Alloy. Compd. 649 (2015) 19–27, https://doi.org/10.1016/j.jallcom.2015.02.124.

[21] F.C. Liu, Z.Y. Ma, Influence of tool dimension and welding parameters on microstructure and mechanical properties of friction–stir–welded 6061–T651 aluminum alloy, Metall. Mater. Trans. A 39 (2008) 2378–2388, https://doi.org/10.1007/s11661-008-9586-2.

[22] Z.Y. Ma, A.H. Feng, D.L. Chen, J. Shen, Recent advances in friction stir welding/processing of aluminum alloys: microstructural evolution and mechanical properties, Crit. Rev. Solid State 43 (4) (2018) 269–333, https://doi.org/10.1080/10408436.2017.1358145.

[23] Y. Tao, D.R. Ni, B.L. Xiao, Z.Y. Ma, W. Wu, R.X. Zhang, Y.S. Zeng, Origin of unusual fracture in stirred zone for friction stir welded 2198–T8 Al–Li alloy joints, Mater. Sci. Eng. A 693 (2017) 1–13, https://doi.org/10.1016/j.msea.2017.03.079.

[24] N. Akhtar, S.J. Wu, Macromechanics study of stable fatigue crack growth in Al–Cu–Li–Mg–Ag alloy, Fatigue Fract. Eng. Mater. Struct. 40 (2017) 233–244, https://doi.org/10.1111/ffe.12489.

[25] H. Sidhar, R.S. Mishra, Aging kinetics of friction stir welded Al–Cu–Li–Mg–Ag and Al–Cu–Li–Mg alloys, Mater. Des. 110 (2016) 60–71, https://doi.org/10.1016/j.matdes.2016.07.126.

[26] W.J. Park, N.J. Kim, Microstructural characterization of 2124 Al–SiC {sub W} composite, Scr. Mater. 36 (1997) 1045–1051, https://doi.org/10.1016/S1359-6462(97)00008-0.

[27] N. Boukos, E. Flouda, C. Papastaikoudis, The effect of Ag additions on the microstructure of aluminium–lithium alloys, J. Mater. Sci. 33 (1998) 3213–3218, https://doi.org/10.1023/A:1004372612504.

[28] K.S. Kumar, S.A. Brown, J.R. Pickens, Microstructural evolution during aging of an AlCuLiAgMgZr alloy, Acta Mater. 44 (1996) 1899–1915, https://doi.org/10.1016/1359-6454(95)00319-3.

[29] B. Noble, G.E. Thompson, T1 (Al2CuLi) precipitation in aluminium–copper–lithium alloys, Metal Sci. J. 6 (1972) 167–174, https://doi.org/10.1179/030634572790445975.

[30] Y. Ma, X. Zhou, G.E. Thompson, T. Hashimoto, P. Thomson, M. Fowles, Distribution of intermetallics in an AA 2099–T8 aluminium alloy extrusion, Mater. Chem. Phys. 126 (2011) 46–53, https://doi.org/10.1016/j.matchemphys.2010.12.014.

[31] D. Khireddine, R. Rahouadj, M. Clavel, Evidence of S′ phase shearing in an aluminium–lithium alloy, Scr. Metall. 22 (1988) 167–172, https://doi.org/10.1016/S0036-9748(88)80327-2.

[32] H.Y. Li, Y. Tang, Z.D. Zeng, Z.Q. Zheng, F. Zheng, Effect of ageing time on strength and microstructures of an Al–Cu–Li–Zn–Mg–Mn–Zr alloy, Mater. Sci. Eng. A 498 (2008) 314–320, https://doi.org/10.1016/j.msea.2008.08.001.

[33] R.D. Schueller, F.E. Wawner, A.K. Sachdev, Nucleation mechanism of the cubic σ phase in squeeze–cast aluminium matrix composites, J. Mater. Sci. 29 (1994) 424–435, https://doi.org/10.1007/BF01162502.

[34] H.K. Hardy, J.M. Silcock, The phase sections at 500 and 350°C of aluminium rich Al–Cu–Li alloys, J. Ins. Met. 84 (1956) 423–428.

[35] S.C. Wang, M.J. Starink, Precipitates and intermetallic phases in precipitation hardening Al–Cu–Mg–(Li) based alloys, Intern. Mater. Rev. 50 (2005) 193–215, https://doi.org/10.1179/174328005X14357.

[36] R.D. Schueller, A.K. Sachdev, F.E. Wawner, Identification of a cubic precipitate observed in an Al–4.3 Cu–2MgSiC cast composite, Scr. Metall. Mater. 27 (1992) 617–622, https://doi.org/10.1016/0956-716X(92)90350-N.

[37] J.M. Silcock, T.J. Heal, H.K. Hardy, Structural ageing characteristics of binary aluminium–copper alloys, J. Ins. Met. 82 (1954) 239–248.

[38] C.J. Tseng, S.L. Lee, S.C. Tsai, C.J. Cheng, Effects of manganese on microstructure and mechanical properties of A206 alloys containing iron, J. Mater. Res. 17 (2002) 2243–2250, https://doi.org/10.1557/JMR.2002.0330.

[39] R.W. Fonda, J.F. Bingert, Precipitation and grain refinement in a 2195 Al friction stir weld, Metall. Mater. Trans. A 37 (2006) 3593–3604, https://doi.org/10.1007/s11661-006-1054-2.

[40] M.J. Starink, N. Gao, N. Kamp, S.C. Wang, P.D. Pitcher, I. Sinclair, Relations between microstructure, precipitation, age–formability and damage tolerance of Al–Cu–Mg–Li (Mn, Zr, Sc) alloys for age forming, Mater. Sci. Eng. A 418 (2006) 241–249, https://doi.org/10.1016/j.msea.2005.11.023.

[41] C. Shi, N.J. Hu, J.C. Huang, Precipitation behaviors in Al–Cu–Mg and 2024 aluminum alloys, Metall. Mater. Trans. A 77 (1996) 2479–2494, https://doi.org/10.1007/BF02652342.

[42] Z.Q. Feng, Y.Q. Yang, B. Huang, X.N. Luo, M.H. Li, Y.X. Chen, M. Han, M.S. Fu, J. Ru, HRTEM and HAADF–STEM tomography investigation of the heterogeneously formed S (Al2CuMg) precipitates in Al–Cu–Mg alloy, Phil. Mag. 93 (2013) 1843–1858, https://doi.org/10.1080/14786435.2012.762469.

[43] T. Sato, S. Hirosawa, K. Hirose, T. Maeguchi, Roles of microalloying elements on the cluster formation in the initial stage of phase decomposition of Al–based alloys, Metal. Mater. Trans. A 34 (2003) 2745–2755, https://doi.org/10.1007/s11661-003-0176-z.

[44] A.K. Mukhopadhyay, Coprecipitation of Ω and σ phases in Al–Cu–Mg–Mn alloys containing Ag and Si, Metal. Mater. Trans. A 33 (2002) 3635–3648, https://doi.org/10.1007/s11661-002-0238-7.

[45] L. Reich, S.P. Ringer, K. Hono, Origin of the initial rapid age hardening in an Al–1.7 at.% Mg–1.1 at.% Cu alloy, Phil. Mag. Lett. 79 (1999) 639–648, https://doi.org/10.1080/095008399176689.

[46] A. Luo, D.J. Lloyd, A. Gupta, W.V. Youdelis, Precipitation and dissolution kinetics in Al–Li–Cu–Mg alloy 8090, Acta Mater. 41 (1993) 769–776, https://doi.org/10.1016/0956-7151(93)90009-H.

[47] K.S. Prasad, A.K. Mukhopadhyay, A.A. Gokhale, D. Banerjee, D.B. Goel, σ precipitation in an Al–Li–Cu–Mg–Zr alloy, Scr. Metall. Mater. 30 (1994) 1299–1304, https://doi.org/10.1016/0956-716X(94)90262-3.

[48] A. Deschamps, M. Garcia, J. Chevy, B. Davo, F. De Geuser, Influence of Mg and Li content on the microstructure evolution of Al–Cu–Li alloys during long–term ageing, Acta Mater. 122 (2017) 32–46, https://doi.org/10.1016/j.actamat.2016.09.036.

[49] M.X. Milagrea, N.V. Mogilib, U. Donatusa, A.R.G. Rafael, T. Maysa, et al., On the microstructure characterization of the AA2098–T351 alloy welded by FSW, Mater. Charact. 140 (2018) 233–246, https://doi.org/10.1016/j.matchar.2018.04.015.

[50] P.A. Colegrove, H.R. Shercliff, Experimental and numerical analysis of aluminium alloy 7075–T7351 friction stir welds, Sci. Technol. Weld Joi. 8 (2003) 360–368 9/136217103225005534 https://doi.org/10.1179/136217103225005534.

[51] R.D. Schueller, A.K. Sachdev, F.E. Wawner, Identification of a cubic precipitate observed in an AL–4.3Cu–2MgSiC cast composite, Scr. Metall. Mater. 27 (1992) 617–622, https://doi.org/10.1016/0956-716X(92)90350-N.

[52] J.A. Walsh, K.V. Jata, E.A. Starke Jr., The influence of Mn dispersoid content and stress state on ductile fracture of 2134 type Al alloys, Acta Metall. 37 (1989) 2861–2871, https://doi.org/10.1016/S0001-6160(89)80001-X.

[53] M. Sugamata, C.P. Blankenship Jr., E.A. Starke Jr., Predicting plane strain fracture toughness of Al–Li–Cu–Mg alloys, Mater. Sci. Eng. A 163 (1993) 1–10, https://doi.org/10.1016/0921-5093(93)90572-V.

[54] W.A. Tayon, K.E. Nygren, R.E. Crooks, D.C. Pagan, In–situ study of planar slip in a commercial aluminum–lithium alloy using high energy X–ray diffraction microscopy, Acta Mater. 173 (2019) 231–241, https://doi.org/10.1016/j.actamat.2019.04.030.

[55] S. Kalyanam, J. Beaudoin, R.H. Dodds Jr., F. Barlat, Delamination cracking in advanced aluminum–lithium alloys–experimental and computational studies, Eng. Fract. Mech. 76 (2009) 2174–2191, https://doi.org/10.1016/j.engfracmech.2009.06.010.